Coronal flux ropes and their interplanetary counterparts

N. Gopalswamy [a,*], S. Akiyama [a,b], S. Yashiro [a,b], H. Xie [a,b]

[a] *NASA Goddard Space Flight Center Greenbelt, MD, 20771, USA*
[b] *The Catholic University of America, Washington DC, 20064, USA*

ARTICLE INFO

ABSTRACT

We report on a study comparing coronal flux ropes inferred from eruption data with their interplanetary counterparts constructed from in situ data. The eruption data include the source-region magnetic field, post-eruption arcades, and coronal mass ejections (CMEs). Flux ropes were fit to the interplanetary CMEs (ICMEs) considered for the 2011 and 2012 Coordinated Data Analysis Workshops (CDAWs). We computed the total reconnected flux involved in each of the associated solar eruptions and found it to be closely related to flare properties, CME kinematics, and ICME properties. By fitting flux ropes to the white-light coronagraph data, we obtained the geometric properties of the flux ropes and added magnetic properties derived from the reconnected flux. We found that the CME magnetic field in the corona is significantly higher than the ambient magnetic field at a given heliocentric distance. The radial dependence of the flux-rope magnetic field strength is faster than that of the ambient magnetic field. The magnetic field strength of the coronal flux ropes is also correlated with that in interplanetary flux ropes constructed from in situ data, and with the observed peak magnetic field strength in ICMEs. The physical reason for the observed correlation between the peak field strength in ICMEs is the higher magnetic field content in faster coronal flux ropes and ultimately the higher reconnected flux in the eruption region. The magnetic flux ropes constructed from the eruption data and coronagraph observations provide a realistic input that can be used by various models to predict the magnetic properties of ICMEs at Earth and other destination in the heliosphere.

1. Introduction

Coronal mass ejections (CMEs) are one of the most important players in solar terrestrial relationship owing to their ability to cause intense geomagnetic storms and large solar energetic particle events (see e.g., Zhang et al., 2007; Gopalswamy, 2009; 2010a). CMEs that continue into the heliosphere to become interplanetary CMEs (ICMEs) are on average fast and wide (Gopalswamy et al., 2010a). In other words, CMEs surviving far into the IP medium are generally more energetic. The energy of the CMEs can be traced to the free energy available in source magnetic regions on the Sun. Weak correlation between CME speed and the free energy available in the source regions has been reported (Gopalswamy et al., 2010a; Gopalswamy, 2011) based on the assumption that the magnetic potential energy is a good proxy to the free energy (Mackay et al., 1997; Forbes, 2000; Metcalf et al., 1995). A close connection between CMEs and flares is also expected based on the standard eruption model known as the Carmichael – Sturrock – Hirayama – Kopp and Pnueman (CSHKP) model (Carmichael, 1964; Sturrock, 1966; Hirayama, 1974; Kopp and Pneuman, 1976). The model involves the formation and

ejection of a plasmoid with simultaneous formation of a post eruption arcade (PEA) due to RC. In three dimensions, the plasmoid is a flux rope (see e.g., Shibata et al., 1995; Longcope et al., 2007).

Soft X-ray emission from PEAs represents the flare, while the ejected flux ropes represent the CME. Thus a close connection between CMEs and flares is expected except in confined flares, which do not involve any mass motion (Gopalswamy et al., 2009a). Correlating flare energy and CME kinetic energy with the active region potential energy neglects some key details of an eruption. For example, eruptions generally do not cover the entire active region area. It is well known that when there are multiple neutral lines present in an active region, eruptions can occur at different neutral lines at different times showing very different PEA morphologies. A well-known example is the two extreme events on 2003 October 28 and 29 that occurred on two different neutral lines in active region 10486. Accordingly, the PEA of the October 28 event formed over a horizontal neutral line, while the October 29 PEA was predominantly in the north-south direction because of the near-vertical neutral line involved (Gopalswamy et al., 2005a; Gopalswamy, 2008). Therefore, it important to consider only that section of the active region that underlies

the PEA. Secondly, the PEA "matures" in the decay phase of the flare, and hence incorporates the time evolution of the eruption. Thus the total reconnected flux in the source region should be a better eruption characteristic that should be closely related to the flare fluence and the CME speed (or kinetic energy).

Longcope et al. (2007) showed that the PEA and flux rope are natural products of the reconnection process, so the poloidal flux of the flux rope should be the same as the reconnected (RC) flux in the source region. It is possible to test this flux relationship using solar and interplanetary data since the ejected flux ropes at the Sun are detected in situ in the solar wind as magnetic clouds (MCs) (Burlaga et al., 1981; Goldstein, 1983; Klein and Burlaga, 1982). Qiu et al. (2007) confirmed that the RC flux at the Sun is about the same as the poloidal flux of the corresponding MC at 1 au (see also Möstl et al., 2009; Hu et al., 2014; Gopalswamy et al., 2017). Qiu et al. (2007) determined the RC flux as the photospheric magnetic flux underlying the area swept up by the flare ribbons on one side of the polarity inversion line. Gopalswamy et al. (2017) introduced a new method of estimating the reconnected flux based on just PEAs, somewhat similar to the "flare flux" computed by Moore et al. (2007). According to this arcade method, a single image in EUV or X-ray in the decay phase of the flare can be used to estimate the RC flux: half of the magnetic flux underlying the PEA is the RC flux. They confirmed this by comparing the RC flux from both flare-ribbon and the arcade methods. They also confirmed the relation between the RC flux and the poloidal flux of the associated MCs for a larger sample of events than in Qiu et al. (2007).

One of the earliest ideas on CME flux ropes near the Sun was proposed by Mouschovias and Poland (1978) . They successfully applied the flux rope model to a Skylab CME and found reasonable geometrical and magnetic properties of the flux rope. Chen et al. (1997) identified flux rope morphology in white-light CMEs observed by the Solar and Heliospheric Observatory (SOHO, Domingo et al., 1995) mission. Gibson and Low (1998) modeled CMEs with complex three-part structures with a 3D flux rope. Krall and St. Cyr (2006) constructed a three-dimensional flux-rope model and found it to have good match with white-light observations. Krall (2007) further showed that CMEs can be modeled as hollow flux ropes. Thernisien (2011) introduced the graduated cylindrical shell (GCS) model to describe white-light CMEs observed in multiple views using SOHO and the Solar Terrestrial Relations Observatory (STEREO, Kaiser et al., 2008). Xie et al. (2013) applied the elliptical flux rope (EFR) model of Krall and St. Cyr (2006) to show that a flux rope can be fit to white light CME irrespective of their appearance at 1 au as MCs or non-cloud ejecta (EJ).

The idea that all ICMEs have flux rope structure has been confirmed by many studies that show that both MCs and EJs contain flux ropes (Marubashi, 1997; Owens et al., 2005; Gopalswamy et al., 2013a; Xie et al., 2013; Mäkelä et al., 2013; Yashiro et al., 2013; Kim et al., 2013; Marubashi, 2015). Numerical models use flux rope as a fundamental magnetic structure to model CMEs from the Sun to 1 AU (see e.g. Tóth et al., 2007; Jin et al., 2017a). However, a flux rope may not be observed at 1 au when the observing spacecraft does not pass through the axis of the flux rope (Gopalswamy, 2006). Such a situation is expected for CMEs originating at large central meridian distances. However, eruptions originating within a longitudinal distance of 15° also ended up as EJs at 1 au (Gopalswamy et al., 2013a). Examination of such events has revealed that the associated CMEs deflected away from the Sun-Earth line (Xie et al., 2013; Kim et al., 2013) because of the presence of coronal holes near the source regions (Mäkelä et al., 2013). Furthermore, the charge state properties of MC and EJ events were similar, suggesting that both were formed due to reconnection involving flares and flux ropes (Gopalswamy et al., 2013b). Both MC and EJ events were associated with similar PEAs suggesting that the eruption was similar producing PEAs and flux ropes (Yashiro et al., 2013). Finally, Marubashi et al. (2015) were able to fit flux ropes to even EJ events taking into account of the different impact parameters and adjusting the EJ boundaries in the solar wind data.

In this paper, we examine the RC flux in the solar sources of EJ and MC events and compare it with the flare, CME, and ICME properties. This study further confirms that the flux rope is a fundamental structure in all large solar eruptions and that the RC flux helps define the complete properties (geometrical and magnetic) of CME flux ropes near the Sun.

2. Data selection

We make use of the list of 54 eruptions in solar cycle 23 considered for the Flux Rope CDAW workshops (Gopalswamy et al., 2010b, 2013b). Only eruptions occurring from within ±15° in longitude of the disk center were considered to make sure the CMEs reached Earth to be detected by one or more of the Advanced Composition Explorer (ACE, Stone et al., 1998), Wind (Acuña et al., 1995), and SOHO spacecraft. The associated CMEs were observed by the Large Angle and Spectrometric Coronagraph (LASCO, Brueckner et al., 1995). Some ICMEs were consistent with the classical definition of MCs (enhanced field strength, smooth rotation of one of the components and low plasma temperature, see Klein and Burlaga, 1982); those that did not agree with this definition were classified as EJs. For MCs, it was possible to fit a force-free cylindrical flux rope to the in situ solar wind plasma and magnetic field data (e.g., Lepping et al., 1990). The selected MCs can also be found on line with all the fitted parameters listed (http://wind.nasa.gov/mfi/mag_cloud_S1.html). Only 23 of the 54 ICMEs were well-defined MCs and the remaining 31 ICMEs were classified as EJs. However, Marubashi et al. (2015) have shown that it is possible to fit flux ropes even to EJ events. Therefore, we shall retain the EJ and MC labels as in the original list, with the understanding that both MC and EJ events have flux rope structure.

Our aim is to combine the source magnetic properties and the flux-rope geometric properties to fully describe the "magnetized" flux ropes in terms of the axial field strength and the poloidal and toroidal fluxes. In order to do this, we compute the RC flux from source regions using the PEA technique recently developed by Gopalswamy et al. (2017). According to this method, the RC flux is computed as half the unsigned photospheric magnetic flux underlying PEAs in the source region. The RC flux has been taken to be the poloidal flux of the flux rope created during the eruption process as has been demonstrated theoretically (Longcope et al., 2007) and observationally (Qiu et al., 2007; Hu et al., 2014; Gopalswamy et al., 2017). Equating the RC flux to the poloidal flux of the newly formed flux rope at the Sun, we determine the axial field in the coronal flux rope. In addition, we compare the near-Sun flux rope properties with near-Earth properties obtained from Marubashi et al. (2015) flux rope fits to in situ data.

Table 1 lists the properties of the 54 ICMEs from the CDAW list. The event identification number in column 1 corresponds to the original numbers used in the CDAW list (Gopalswamy et al., 2013a; Marubashi et al., 2015). The ICME type given in column 2 is based on the classical definition of magnetic clouds identified and modeled by the Wind Magnetic Field Investigation (MFI, Lepping et al., 1995) team. Other ICMEs are designated as non-cloud ejecta (EJ). The observed date, start time, and the peak magnetic field strength of the ICMEs are given in columns 3, 4, and 5, respectively. Properties of the associated CMEs are given columns 6–11 in the following order: CME date, time, sky-plane width, sky-plane speed (V_{sky}), space speed (V_{sp}), and mass. The space speeds were obtained from the halo CME list available at the CDAW Data Center (https://cdaw.gsfc.nasa.gov/CME_list/halo/halo.html). This list includes only full halo CMEs. For other CMEs, an empirical relation obtained by Gopalswamy et al. (2015a) were used: $V_{sp} = 1.10 \, V_{sky} + 156$ in km/s. The CME mass estimates are as listed in the SOHO/LASCO CME catalog (https://cdaw.gsfc.nasa.gov/CME_list/index.html, Yashiro et al., 2004; Gopalswamy et al., 2009b). For 8 full halo CMEs, the mass estimate is not available. For these, we used an average value of 10^{16} g based on the fact that halo CMEs are generally fast, wide and massive (Gopalswamy et al., 2005b). Properties of the associated flares are listed in columns 12–15: heliographic coordinates of the flare location, GOES soft X-ray flare size, soft X-ray fluence, and the RC flux (Φ_r). The fluence values

Table 1
List of eruptions with ICME, CME, and Flare parameters.

Event #[a]	ICME				CME						Flare				Coronal Flux Rope					1-au FR[h]	
	Type[b]	Date yy/mm/dd	Time UT	B_t nT	Date mm/dd	Time UT	Width deg	V_{sky} km/s	V_{sp} km/s[d]	Mass 10^{15} g	Location	X-ray Size[f]	Fluence 10^{-2} J/m²	Φ_r 10^{21} Mx	Λ	R_{tip} Rs	Direction	V_{spf} km/s[g]	B_0 at 10 Rs mG	Φ_p 10^{21} Mx	B_0 at 1 au nT
1	MC	97/01/10	05:18	–	01/06	15:10	360	136	232	0.58	S18E06	A1.1	–	–	0.95	5.50	S18W01	258	–	3.13	19.0
2	MC	97/05/15	09:06	26.1	05/12	05:30	360	464	749	4.16	N21W08	C1.3	0.25	2.4	1.00	26.00	N01W02	670	17.6	5.32	35.1
3	EJ+	97/12/11	03:45	14.6	12/06	10:27	223	397	592	20.1	N45W10	B7.0	2.16	7.7	1.10	7.80	N15W30	569	61.2	4.21	29.2
4	EJ?	98/05/03	19:00	10.0	05/01	23:40	360	585	866	6.85	S18W05	M1.2	1.60	3.0	0.50	22.50	S01E14	826	14.9	–	–
5	EJ+	98/05/04	10:00	21.0	05/02	14:06	360	938	1168	7.73	S15W15	X1.1	6.70	3.6	0.60	28.50	N08W05	2097	19.5	0.74	8.80
7	EJ+	98/11/07	22:00	16.2	11/04	07:54	360	523	809	6.99	N17W01	C1.6	–	4.1	0.70	23.50	N25W01	706	24.4	5.24	42.4
8	EJ+	98/11/13	04:30	21.3	11/09	18:18	190	325	513	2.84	N15W05	C2.5	0.36	2.5	1.00	9.90	N15W05	712	18.8	5.86	26.1
9	MC	99/04/16	20:18	24.8	04/13	03:30	261	291	476	1.40	N16E00	B4.3	0.07	1.5	0.60	8.00	S02W06	560	8.0	5.35	28.6
10	EJ+	99/06/27	21:30	12.1	06/24	13:31	360	975	1143	2.29	N29W13	C4.1	3.30	5.2	0.70	7.50	N25W15	1531	31.0	0.77	8.70
13	EJ+	99/09/22	21:00	24.6	09/20	06:06	360	604	900	0.89	S20W05	C1.4	–	2.7	1.80	7.80	S20W05	868	30.7	3.05	25.9
14	EJ+	99/10/21	18:30	36.6	10/18	00:06	240	144	314	3.43	S30E15	C1.2	0.09	0.90	1.10	5.50	S30E15	217	7.1	2.08	38.4
15	EJ+	00/01/22	18:00	17.6	01/18	17:54	360	739	1077	6.94	S19E11	M3.9	5.70	7.5	0.70	6.50	S10E29	1179	44.4	2.22	14.3
16	MC	00/02/21	09:48	18.4	02/17	21:30	360	728	973	14.7	S29E07	M1.3	2.70	3.0	0.70	19.50	S12W02	994	17.8	4.56	23.0
17	EJ+	00/07/11	01:30	16.4	07/07	10:26	360	453	766	1.82	N04E00	C4.5	3.45	3.9	1.10	8.50	S17W05	739	30.9	2.66	22.2
18	EJ+	00/07/11	22:48	11.4	07/08	23:50	161	483	687	10.0e	N18W12	C4.0	2.69	7.1	0.90	8.50	N18W06	1152	49.0	7.94	16.7
19	MC	00/07/15	21:06	48.6	07/14	10:54	360	1674	2061	13.9	N22W07	X5.7	75.00	13.1	0.50	6.10	N18W14	2281	65.0	18.0	74.1
20	EJ+	00/07/27	08:28	7.4	07/23	05:30	181	631	850	3.08	S13W05	–	–	1.9	0.80	7.50	S13E04	1119	12.5	0.48	9.80
21	MC	00/07/28	21:06	15.6	07/25	03:30	360	528	900	1.63	N06W08	M8.0	2.80	1.1	0.80	8.50	S15E04	960	7.3	–	–
23	MC	00/08/12	06:06	–	08/09	16:30	360	702	1007	7.02	N20E12	–	1.20	–	1.00	6.50	N17E05	1024	–	9.27	34.9
24	MC	00/09/18	01:54	36.10	09/16	05:18	360	1215	1568	9.59	N14W07	M5.9	9.80	5.5	0.80	11.80	N08W07	1574	35.8	6.96	37.2
25	EJ+	00/10/05	13:13	15.3	10/02	03:50	360	525	877	6.76	S09E07	C4.1	0.55	0.37	1.00	7.10	S19E08	1104	2.7	1.38	10.5
26	MC	00/10/13	18:24	14.1	10/09	23:50	360	527	903	14.3	N01W14	C6.7	1.70	5.1	0.90	7.50	N20W14	1287	35.4	4.35	19.7
27	MC	00/11/06	23:06	24.8	11/03	18:26	360	291	701	4.85	N02W02	C3.2	3.22	14.9	0.80	10.10	N02E05	542	96.2	3.24	25.1
28	EJ+	00/11/27	05:00	24.5	11/24	05:30	360	1289	1611	6.33	N20W05	X2.0	8.30	2.7	0.60	6.80	N30W18	1745	14.7	2.80	23.0
29	EJ+	01/03/04	04:00	13.1	02/28	14:50	232	313	500	2.41	S17W05	B4.2	0.12	2.7	0.70	6.50	S05W15	522	16.0	1.12	12.0
30	EJ+	01/03/22	22:30	8.8	03/19	05:26	360	389	653	1.19	S20W00	PEA	–	1.3	0.70	7.00	N05W10	691	8.0	0.14	18.5
31	EJ+	01/04/11	22:30	35.4	04/09	15:54	360	1192	1482	4.50	S21W04	M7.9	13.00	11.3	0.60	21.40	S09W10	1813	61.7	–	–
32	MC	01/04/12	07:54	20.9	04/10	05:30	360	2411	2940	9.12	S23W09	X2.3	30.00	7.2	0.70	3.40	S23W05	3735	42.6	1.43	44.9
33	MC	01/04/29	01:54	11.2	04/26	12:30	360	1006	1257	10.0e	N20W05	M1.5	5.10	12.0	0.60	8.90	N20W03	1093	65.5	23.9	14.5
34	EJ-	01/08/13	07:00	12.3	08/09	10:30	175	479	682	3.59	N11W14	PEA	–	1.2	1.20	7.00	N02W18	842	9.9	–	–
35	EJ+	01/10/12	03:30	25.4	10/09	11:30	360	973	1156	11.8	S28E08	M1.4	4.00	3.6	0.90	6.00	S28E01	1449	25.1	11.9	35.8
36	MC	02/03/19	22:54	15.6	03/15	23:06	360	957	1297	22.5	S08W03	M2.2	13.00	11.5	0.60	14.10	N15W01	1151	62.5	–	–
37	MC	02/04/18	04:18	14.5	04/15	03:50	360	720	1143	1.93	S15W01	M1.2	7.10	10.8	0.60	24.00	S01W05	1302	59.0	5.63	23.7
38	EJ+	02/05/11	13:00	20.9	05/08	13:50	360	614	990	0.58	S12W07	C4.2	1.20	2.9	0.90	6.40	S12W05	1231	20.3	0.63	22.3
39	MC	02/05/19	03:54	20.4	05/16	00:50	360	600	823	4.25	S23E15	C4.5	1.50	4.7	1.10	25.10	S23E05	900	37.6	4.69	28.5
40	EJ-	02/05/20	11:00	–	05/17	01:27	45	461	663	1.56	S20E14	–	–	–	1.80	7.50	S28E20	743	–	1.64	12.0
41	EJ-	02/05/30	07:09	8.8	05/27	13:27	161	1106	1372	3.24	N22E15	C3.7	1.50	3.1	0.90	22.40	N32E20	1362	21.5	–	–
42	EJ+	02/07/18	12:00	6.6	07/15	21:30	188	1300	1586	18.7	N19W01	M1.8	4.30	8.2	0.50	5.80	N29E15	2046	40.5	–	–
43	MC	02/08/01	11:54	14.9	07/29	12:07	161	222c	400	8.44	S10W10	M4.7	8.50	10.2	0.80	7.50	S02W10	1134	65.8	1.99	20.9
44	MC	03/08/18	11:36	20.2	08/14	20:06	360	378	766	10.0e	S10E02	C3.8	1.63	10.9	1.10	8.80	N12E10	662	86.2	2.67	19.8
45	MC	03/10/29	08:00	48.4	10/28	11:30	360	2459	3128	10.0e	S16E08	X17.2	170.00	20.8	0.50	4.10	S16E20	2916	103.0	23.9	69.5
46	MC	03/10/31	02:00	35.9	10/29	20:54	360	2029	2628	16.6	S15W02	X10.0	87.00	21.6	0.50	4.00	S15E05	3474	107.2	7.58	40.5
47	EJ+	04/01/22	08:00	30.1	01/20	00:06	360	965	1248	10.1	S13W09	C5.5	4.60	14.0	0.90	7.80	S25W10	1441	97.0	9.60	22.7
48	MC	04/07/24	12:48	–	07/22	08:30	132	899	1144	0.73	N04E10	C5.3	0.56	–	0.70	7.80	N06E05	1359	–	5.35	38.6
49	MC	04/11/09	20:54	41.6	11/06	02:06	214	1111	1378	5.96	N09E05	M3.6	5.50	6.7	0.50	31.80	N07W00	1319	33.3	–	–
50	EJ+	04/12/12	12:00	15.8	12/08	20:26	360	611	1109	5.32	N05W03	C2.5	0.74	2.2	0.60	6.50	S05W06	754	12.0	4.42	20.9
51	EJ+	05/01/16	14:00	11.0	01/15	06:30	360	2049	2701	10.0e	N16E04	M8.6	29.00	20.8	0.90	6.10	N25W01	2503	144.6	1.15	11.8
52	EJ+	05/02/18	15:00	9.0	02/13	11:06	151	584	798	1.10	S11E09	C2.7	0.22	0.56	0.85	6.10	S21E19	587	0.4	2.71	9.60
53	MC	05/05/15	05:42	56.1	05/13	17:12	360	1689	2171	10.0e	N12E11	M8.0	18.00	9.7	0.50	7.50	N05E11	2384	33.3	20.3	79.0
54	MC	05/05/20	07:18	15.5	05/17	03:26	273	449	649	10.0e	S15W00	M1.8	1.50	2.6	0.70	7.50	N08W01	569	15.3	2.22	19.8
56	EJ+	05/07/10	10:30	25.0	07/07	17:06	360	683	1173	10.0e	N09E03	M4.9	5.30	4.9	1.10	8.90	N12E26	1040	39.0	–	–
57	EJ+	05/09/02	19:03	15.6	08/31	11:30	360	825	1283	2.39	N13W13	C2.0	1.20	4.8	0.90	24.50	N08W25	1161	33.1	–	–
58	EJ+	05/09/15	14:24	–	09/13	20:00	360	1866	2445	18.7	S09E10	X1.5	55.00	–	0.60	5.90	S29E21	2171	–	–	–
59	EJ+	06/08/20	00:00	15.6	08/16	16:30	360	888	1359	10.1	S16W08	C3.6	3.60	3.3	0.70	8.30	S28W01	1351	19.7	–	–

The list contains 54 events out of the original 59 events because
#6, #12, #55 Dropped from the analysis because the revised solar source location fell outside the longitude criterion.
#11 Dropped from the analysis because this is a known "driverless" event.
#22 Dropped from the analysis because of the uncertainty in identifying the solar source; multiple candidate eruptions exist.

[a] List of ICMEs during solar cycle 23 with solar sources near Disk Center (E15° ≤ source longitude ≤ W15°) (from Gopalswamy et al., 2010, 2013).

[b] MC = Magnetic cloud; EJ = Ejecta; the suffix + indicates that it was possible fit a flux rope to the ejecta by adjusting the plasmag boundaries; - indicates it was not possible to fit a flux rope.

[c] Incorrect feature might have been tracked to get the speed.

[d] Deprojected speed using cone model (for full halo CMEs) or from the empirical relation in Gopalswamy et al. (2015a) for non-halo CMEs.

[e] Assumed mass values.

[f] EP = Eruptive prominence; PEA = post-eruption arcade.

[g] Space speed obtained by tracking the leading edge of flux ropes.

[h] 1-au flux rope properties B_0 and R_0 are from Marubashi et al. (2015); the poloidal flux at 1 au was computed from B_0 and R_0.

were taken from the Solar Geophysical Data for most of the events; for some events (especially the ones associated with eruptive prominences) the fluence was not listed, so we computed it from the GOES soft X-ray flux. Φ_r was determined from the PEA method, which is half the sum of

photospheric magnetic flux in each pixel in the area underlying the PEA (Gopalswamy et al., 2017). Xie et al. (2013) applied the EFR model to the white light images obtained by SOHO/LASCO using its C2 and C3 telescopes. This model assumes that the CME flux rope has an elliptical axis

with varying radial circular cross-section. The aspect ratio is the main geometrical parameter related to Λ, the ratio of the heliocentric distance to the radius (R_0) of the flux rope at its apex. In terms of the heliocentric distance (R_{tip}) to the tip of the flux rope, $\Lambda = \frac{1}{2} (R_{tip} - R_0)/R_0$. The Λ parameter obtained from the EFR fits is given in column 16 while the R_{tip} values used in computing Λ are given in column 17. The flux rope fit also gives the direction of the flux rope (column 18), which can be different from the flare location because of non-radial motion of the flux rope (Gopalswamy et al., 2009c; Xie et al., 2013; Mäkelä et al., 2013; Gopalswamy et al., 2014a). By tracking the leading edge of the flux rope, we also get the deprojected speed of the flux rope (V_{spf}) given in column 18 giving another estimate of the space speed listed in column 10. Under the assumption of self-similar expansion and the known result that the flare RC flux is approximately the same as the poloidal flux of the flux rope formed due to reconnection, we obtain the axial magnetic field strength of the flux rope in the corona as $B_0 = \Phi_r x_{01}/LR_0$, where x_{01} is the first zero of the Bessel function J_0 and L is the length of the flux rope taken as $2R_{tip}$. We can calculate B_0 at any distance, but we have listed the value at 10 Rs in column 20 in units of mG. Marubashi et al. (2015) fitted flux ropes to the 1-au data of to both MC and EJ events giving flux rope parameters such as the axial field strength B_0 and radius R_0 at 1 au. From these, we determined the poloidal flux of the 1-au flux ropes as Φ_p (1 au) $= LB_0 R_0/x_{01}$. We assumed the flux rope length L to be 2 au at Earth. In four ICMEs Marubashi et al. (2015) had to split the ICMEs into more than one flux rope to do the fits. We excluded these ICMEs in this study. The resulting Φ_p (1 au) and B_0 (1 au) are listed in columns 21 and 22, respectively. We use the data in Table 1 to relate the eruption data to the coronal and interplanetary flux rope properties.

3. RC flux and flare properties

Fig. 1 shows the solar source of one of the events in Table 1 (#10, 1999 June 24). The eruption was characterized by a two-ribbon flare observed in H-alpha and a PEA centered at N29W13 observed by Yohkoh's Soft X-ray Telescope (SXT, Tsuneta et al., 1991) and SOHO's Extreme-ultraviolet Imaging Telescope (EIT, Delaboudinière et al.,
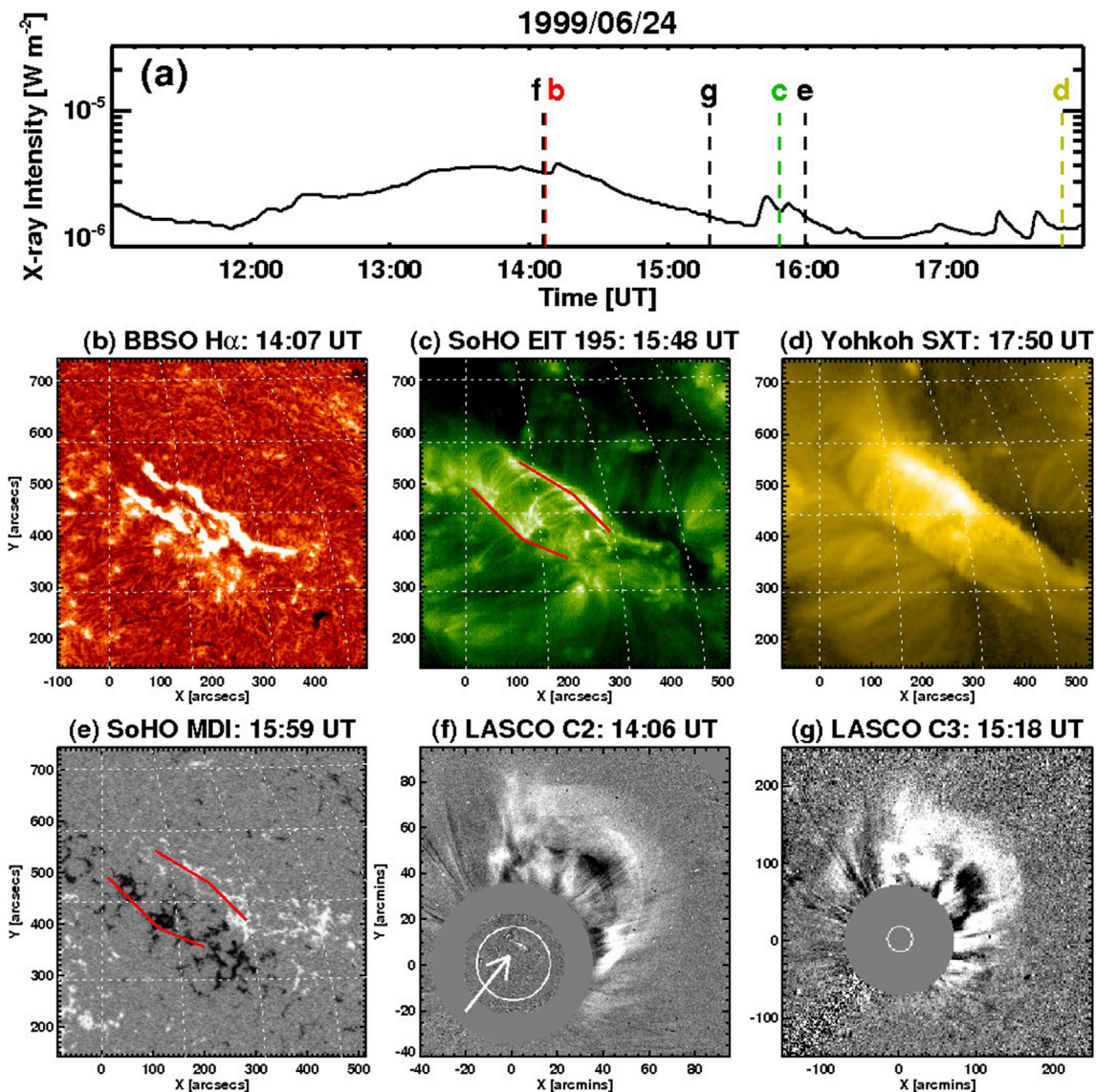
Fig. 1. The solar source, flare, and CME in the 1999 June 24 eruption. (a) GOES soft x-ray light curve in the 1–8 Å band showing the C4.1 gradual flare associated with the eruption. (b) H-alpha picture from the Big Bear Solar Observatory (BBSO) showing the two ribbon flare. (c) The post eruption arcade (PEA) observed in EUV by SOHO/EIT in the 195 Å waveband with the footpoints of the arcade marked by the red lines, (d) The PEA observed Yohkoh's Soft X-ray Telescope (SXT), (e) the PEA footpoints superposed on a SOHO/MDI magnetogram taken at 15:59 UT, (f) a SOHO/LASCO difference image at 14:06 UT with a EIT 195 Å difference image superposed showing the CME and the solar source (pointed by arrow), and (g) a SOHO/LASCO/C3 difference showing that the CME became a full halo. The times of various images are marked on the GOES plot in (a) (not in chronological order). (For interpretation of the references to colour in this figure legend, the reader is referred to the web version of this article.)

1995). The PEA was quite extended in the northeast-southwest direction and was formed due to the eruption of a filament (also reported as a disappearing solar filament event from N33E09 during 10:51 to 14:18 UT in the Solar Geophysical Data). In soft X-rays, the flare was of C4.1 class observed by GOES and had a fluence of 3.3×10^{-2} J m^{-2}. The eruptive filament became the core of a large CME observed by SOHO/LASCO. The CME was relatively fast with an average speed of ~975 km/s in the SOHO/LASCO field of view (FOV) and showed a positive acceleration (32.5 m s^{-2}) in the corona, typical of CMEs associated with quiescent filament eruption (Gopalswamy et al., 2015b). By the time the CME reached the edge of the LASCO FOV, it had a speed of 1200 km/s. The CME was a partial halo in the C2 FOV and became a full halo in the C3 FOV. When projection corrected using the cone model (Xie et al., 2004), the CME had an average speed of 1143 km/s. From the leading edge measurements of the flux rope obtained from the EFR model, the space speed was ~1543 km/s. The aspect ratio parameter Λ was 0.70 at an R_{tip} of 7.5 Rs. The flux rope direction (N25W15) was slightly different from the direction indicated by the flare location.

The PEA was superposed on a magnetogram obtained by the Michelson Doppler Imager (MDI, Scherrer et al., 1995) at 15:59 UT to get the RC flux of 5.2×10^{21} Mx. The ICME was an EJ event arriving at Sun-Earth L1 on 1999 June 27 at 21:30 UT. The fitted value of B_0 from Marubashi et al. (2015) was ~8.7 nT and Φ_p (1 au) ~ 0.77×10^{21} Mx. The observed maximum value of the ICME magnetic field was ~12.1 nT. All these parameters compiled for this event can be found in Table 1. Comparing the PEA between EIT and SXT images, we see that the SXT arcade has an extension to the south, which is not clear in the EIT image. When we include the additional area seen in SXT image, we get an RC flux of 7.6×10^{21} Mx, which is larger than the value obtained from EIT by 46%. We decided to stay with the EIT data for consistency because we do not have SXT observations for all the events.

3.1. The RC flux, flare size, and flare fluence

The RC flux from a source region depends on the total amount of magnetic flux involved in an eruption. Observationally, the RC flux is given by the area swept up by the flare ribbons (or the PEA) on one side of the polarity inversion line in the source region and the photospheric magnetic flux under this area. On the other hand the peak soft X-ray flux

and the fluence are due to the hot flare plasma generated as a result of electrons accelerated during the reconnection and precipitating in the solar atmosphere. Therefore, we do expect that the RC flux is related to the flare intensity and fluence. Fig. 2 shows this relationship for all the events in Table 1 that have these measurements. We see that both the flare size and fluence have high correlation with the RC flux. The fluence and flare size vary by more than three orders of magnitude, while the RC flux varies over two orders of magnitude. There is very good overlap between MC and EJ events, suggesting that there is no notable difference in fluences and flare sizes of the two ICME populations. The fluence – RC flux correlation is much stronger because both quantities refer to the total duration of the eruption, while the flare size corresponds to one instance without considering the rise and decay phases.

3.2. The RC flux and CME properties

In an earlier work connecting CME widths and the flare flux, Moore et al. (2007) showed that the CME width is decided by the average magnetic field strength under the flare arcade. Since the RC flux is proportional to the average field strength under the arcade, we do expect a correlation between the RC flux and CME width. However, there is a problem in measuring the CME widths for the events in Table 1: the CMEs are all disk-centered, so most of them are halo CMEs and hence their widths are known from single-view observations. Since the white-light CMEs were fit to a flux rope, we do have the edge-on (W_{edge}) and face-on (W_{face}) widths of the CME flux ropes. We use the quantity $(W_{edge} \times W_{face})^{1/2}$ as a measure of the CME width. We do have good CME speed measurements in the sky plane. As noted in section 2, we do have space speeds from cone model deprojection and flux rope tracking.

Fig. 3 shows that the CME speed is well correlated with the RC flux for both EJ and MC events suggesting that one cannot easily distinguish the two populations based on the CME speeds. We have shown the correlations using space speeds obtained by the cone-model deprojection (Fig. 3a) and flux-rope tracking methods (Fig. 3b). The correlations in Fig. 3a and b are quite similar because the two speeds agree quite well. In Fig. 3c, we have shown the correlation between the RC flux and the flux-rope width defined as $(W_{edge} \times W_{face})^{1/2}$. We see a significant correlation for all events (r = 0.31, r_c = 0.238) and for MC events (r = 0.42, r_c = 0.378). The correlation is also positive in the case of EJ events, but it
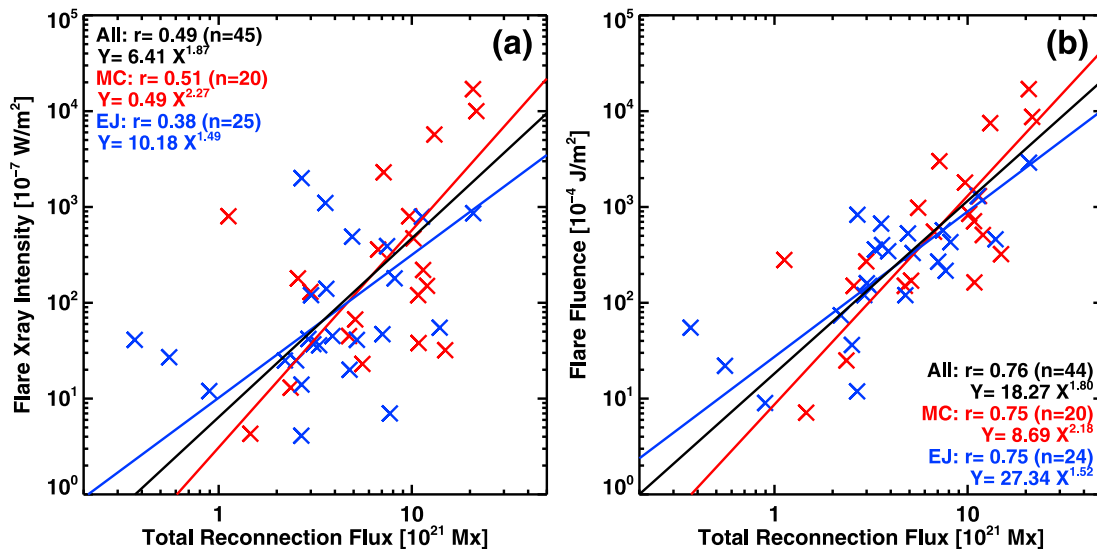

Fig. 2. Scatter plot between the RC flux and (a) the soft X-ray flare size and (b) the soft X-ray flare fluence. The red and blue data points (with the corresponding regression lines) denote flares associated with MCs and EJs, respectively at 1 au. The black line is the regression of the combined data set ("All"). This color-coding is used throughout this paper to distinguish the MC, EJ, and combined data set. The correlation coefficients (r) and the number of data points (n) are shown on the plots. In the RC flux – flare size correlation, the Pearson's critical correlation coefficients (r_c) at 95% confidence level are: 0.251 (All), 0.389 (MC), and 0.337 (EJ); in the RC flux – flare fluence correlation, the critical coefficients at 95% confidence level are: 0.254 (all), 0.389 (MC), and 0.344 (EJ). In both cases, the probability that the correlations for the combined set is by chance is less than 5×10^{-4}. The r_c values quoted throughout this paper correspond to 95% confidence level. (For interpretation of the references to colour in this figure legend, the reader is referred to the web version of this article.)
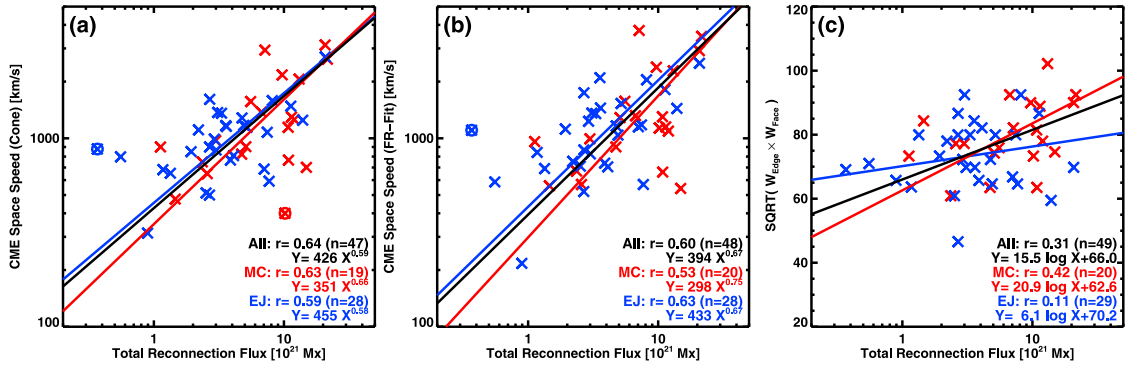
Fig. 3. Scatter plot between CME speed and RC flux for MC (red) and EJ (blue) events: (a) when space speed was determined by correcting the sky-plane speed for projection effects using the cone model and (b) when space speed was obtained by tracking the leading edge of the flux rope. In (a) and (b) event #25 (2000 October 2) is excluded from the correlations because the arcade is ill-defined. Event #43 (2002 July 29) is excluded from (a) because of the large discrepancy between the cone model speed (400 km/s) and the flux-rope speed (1134 km/s). It is possible that the LASCO speed measurement is incorrect. The two excluded data points are shown circled. (c) Scatter plot between the RC flux and the flux rope width obtained as a geometrical mean of the edge-on and face on width (see Xie et al., 2013). All correlations are significant because the Pearson critical values of the correlation coefficients are much smaller. (For interpretation of the references to colour in this figure legend, the reader is referred to the web version of this article.)

is not statistically significant.

The correlation of RC flux with CME speed and width implies that it should also be correlated with the CME kinetic energy. It is well known that the CME mass (M) is related to CME width (W) according to: log $M = 12.6 + 1.3\log W$ (Gopalswamy et al., 2005b). Furthermore, the CME width is also correlated with CME speed (Gopalswamy et al., 2014b). Accordingly, we expect a better correlation between RC flux and CME kinetic energy. Mass estimates are available only for 40 events, which we combined with the space speed from the two methods (cone model and flux rope fit) to get kinetic energies. The SOHO/LASCO catalog lists mass values for CME widths in the range 20–120°. For nine events, we assumed an average mass of 10^{16} g based on the fact that CMEs associated with ICMEs are generally faster and wider on average and a majority of them are halo CMEs. Furthermore, a compilation of masses of limb CMEs indicates that the bin with ~10^{16} g corresponds to above average values (Gopalswamy, 2010a).

The scatter plot between RC flux and CME kinetic energy in Fig. 4 shows that the two quantities have a better correlation than the RC flux – speed correlation. Comparing the kinetic energies obtained from the cone-model and flux-rope tracking speeds, we see that the correlation from the flux-rope tracking is slightly better. The correlations are significant for EJs (r = 0.74, r_c = 0.317 for 28 events), MCs (r = 0.63,

r_c = 0.378 for 20 events) and the combined set (r = 0.71, r_c = 0.243 for 48 events) at 95% confidence level. These numbers include the 8 events for which the mass was assumed. Inclusion of the assumed-mass events did not change the correlation significantly, but does indicate consistency with the measured masses.

4. Flux rope magnetic field in the corona and IP medium

In this section we consider the magnetic field strength in the coronal and in the 1-au flux ropes using independent measurements. We assume force-free flux ropes in both cases. The 1-au flux rope parameters are listed in Marubashi et al. (2015). The magnetic field strength in coronal flux ropes is obtained from a combination of EFR model for geometrical properties and the RC flux computation using the arcade method. We also compare the properties of coronal flux ropes from the source regions of MC and EJ events.

4.1. CME magnetic field strength in coronal flux ropes

One of the immediate outcomes of the close relation between the RC flux and the poloidal flux of the erupted flux rope is that we can obtain the axial field strength (B_0) of the CME flux rope. Using the Lundquist
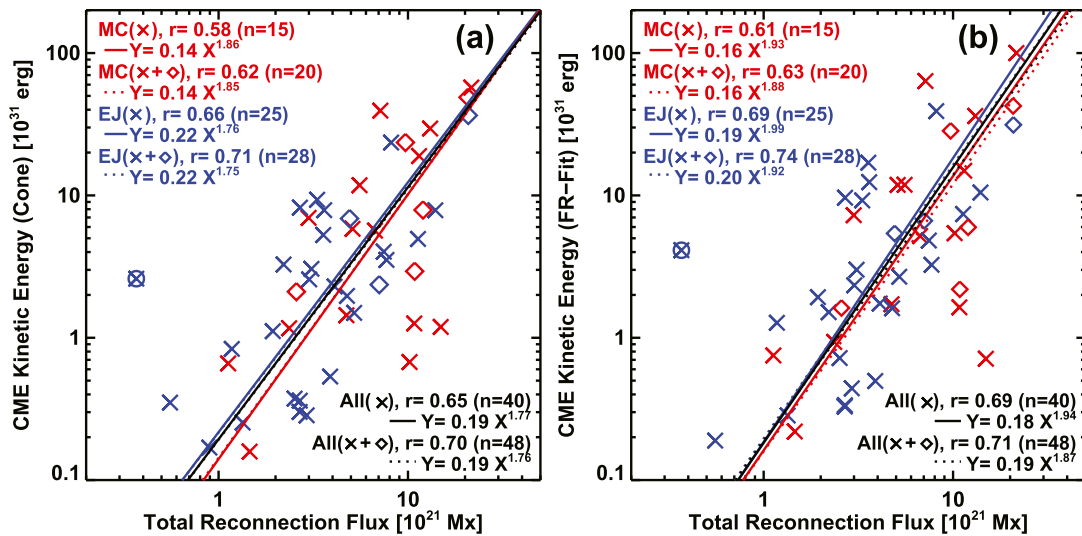
Fig. 4. Scatter plot between CME kinetic energy and RC flux. The kinetic energy was calculated from the CME mass listed in the SOHO/LASCO catalog and the space speed derived from the cone model deprojection (a) or from flux rope fits to the white-light CME data (b). The kinetic energy values obtained by assuming CME mass (10^{16} g for 5 MC events and 3 EJ events) are denoted by diamond symbols. Correlation coefficients and regression lines are shown with and without the few assumed masses. The regression lines are all very close to each other. All the correlation coefficients are much larger than the Pearson correlation coefficient and hence are statistically significant. Event #25 is excluded (data point shown circled) for the reason stated in Fig. 3.

solution for a force free flux rope, we get $B_0 = \Phi_r x_{01}/R_0 L = \Phi_r x_{01}/2R_0^2(2\Lambda + 1)$. Here we have assumed that the poloidal flux of the flux rope in the corona equals the RC flux Φ_r. Fig. 5 (a,b) show histograms of the RC flux in the source regions of MCs and EJs; the distributions have different shapes, even though the range of values is similar. The RC flux in the MC source regions is almost twice that in EJ source regions on average. Fig. 5 (c,d) show the radius (R_0) of the coronal flux rope, which has similar distributions for MC- and EJ-associated CMEs. The distributions of the aspect ratio parameter Λ is also similar for MC and EJ cases (not shown). The axial magnetic field strength B_0 of the white-light flux ropes derived from the RC flux and the fitted flux rope parameters is given in Fig. 5(e and f). We see that the coronal flux rope B_0 values are in MC and EJ events: the average B_0 of MC-associated CME flux ropes is about 65% higher than that in EJ-associated ones. Kolmogorov-Smirnov tests confirmed that distributions of both the RC flux and B_0 have statistically significant differences between MC and EJ events, while the difference in R_0 (and Λ) is not significant. Similar R_0 between MC and EJ events implies that the different Φ_r should lead to different B_0 because $\Phi_r \sim B_0 R_0$ and $R_0 \sim$ constant between MC and EJ events for a given heliocentric distance.

In an early work on CME flux ropes, Mouschovias and Poland (1978) showed that the thickness of the flux rope at the leading edge (and hence the flux rope radius) is proportional to the heliocentric distance of the flux rope ($R_0 \propto R_{tip}$). Since $L = 2 R_{tip}$, we see that $B_0 \sim R^{-2}_{tip}$. This inverse square dependence on distance is faster than that for the background magnetic field in the corona obtained from various techniques. Gopalswamy and Yashiro (2011) determined the variation of the background magnetic field as a function of radial distance from shock standoff distance measured in white-light coronagraph images. They found a relationship $B (R) = 0.356\ R^{-1.28}$ for an adiabatic index of 5/3. For $R = 10\ Rs$, this relation yields a $B = 18.7\ mG$. Clearly, the coronal flux rope has a higher magnetic field strength (by a factor of 2.8 for MCs and 1.8 for EJs) than in the background corona. This is an important

confirmation of the flux-rope nature of CMEs as a low-beta plasma throughout the inner heliosphere. The faster dependence of the flux-rope magnetic field compared to that in the background medium was also found in the specific event investigated by Mouschovias and Poland (1978). Here we are able to confirm that result statistically.

4.2. Flux rope magnetic field strengths at the sun and at 1 au

Two-point measurements (one near the Sun by remote-sensing and the other near Earth by in situ measurements) of solar disturbances have been extremely useful in understanding the propagation of CMEs (Lindsay et al., 1999; Gopalswamy et al., 2000, 2001). Such studies mainly deal with the arrival time and speed of CMEs at 1 au based on CME kinematics at the Sun. A more realistic comparison requires predicting the magnetic properties of ICMEs, which are important for space weather applications. For example, a knowledge of the out-of-the ecliptic component of the magnetic field in ICMEs is critical in predicting the strength of geomagnetic storms (e.g., Wilson, 1987; Gonzalez and Tsurutani, 1987; Wu and Lepping, 2002; Zhang et al., 2007; Gopalswamy et al., 2008; Gopalswamy, 2010b). The flux-rope nature of ICMEs, if known ahead of time, will tell us when and where the southward component of the magnetic field would occur; the product of the southward field component and the ICME speed is the critical in predicting the strength of the resulting geomagnetic storms. The close relation between the RC flux in the source region and the poloidal flux of 1-au MCs thus provides the required link between geomagnetic storms and solar source regions and supports data-constrained CME models (Jin et al., 2017b). We showed in Figs. 3 and 4 that the RC flux has good correlation with CME speed and kinetic energy. We now show that the RC flux has also a reasonable correlation with the 1-au poloidal flux for both MC and EJ events.

Since Marubashi et al. (2015) were able to fit flux ropes to both MC and EJ events, we use the fitted parameters (axial field strength B_0 and
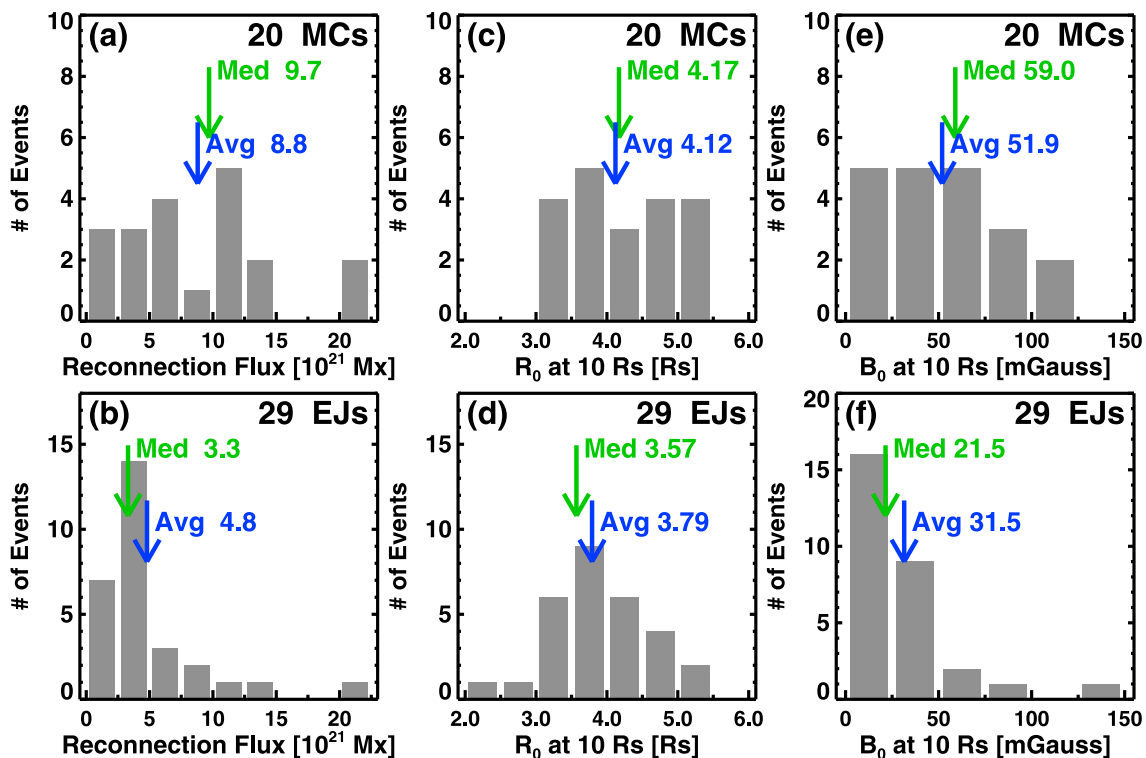
Fig. 5. Distributions of the RC flux Φ_r (a,b), the flux-rope radius R_0 (c,d), and the derived axial magnetic field strength B_0 of the flux rope at a heliocentric distance of 10 Rs (e,f). The top and bottom panels show the quantities associated with MCs and EJs, respectively. The mean (Avg) and median (Med) values are indicated on the plots. Kolmogorov-Smirnov Test comparing the MC and EJ parameters yielded the D-statistic as 0.4241 (RC flux), 0.3017 (R_0) and 0.4741 (B_0). The corresponding probabilities (p) that the obtained D value is by chance are 0.019, 0.191, and 0.006, indicating that R_0 has a similar distribution in MCs and EJs, while the RC flux and B_0 have different distributions.

the flux rope radius R_0 at 1 au) of the flux ropes to obtain the poloidal flux at 1 au as $(L/x_{01})B_0R_0$. Here we assumed the length of the flux rope to be 2 au as in Gopalswamy et al. (2017). As we noted before, we consider only those events that were not split into multiple ICMEs in fitting flux ropes. There are 46 such events, whose 1-au properties are shown in Fig. 6. We see that B_0 of the 1-au flux ropes is higher in MCs by a factor of ~1.5 than in EJs (Fig. 6c), similar to what was found for coronal flux ropes. The poloidal flux derived from the 1-au fits also differ between MC and EJ events (Fig. 6a): the MC poloidal flux is ~73% higher on average. However, the radial size of the flux ropes are not too different. We confirmed that the differences in B_0 and poloidal flux between MC and EJ events are statistically significant, while the difference in R_0 is marginal. The EJ-type ICMEs seem to have flux ropes with smaller magnetic content (lower axial field strength and poloidal flux) compared to MCs. Thus we conclude that there are significant differences between the flux ropes underlying MC and EJ events, the root cause being the different RC fluxes. We also notice that the difference in R_0 at 1 au between EJ and MC is slightly more pronounced than in the corona. This is consistent with the higher magnetic content of MC flux ropes (and hence higher magnetic pressure) resulting in greater expansion and hence relatively a larger size at 1 au.

Fig. 7a shows the relation between the RC flux and the poloidal flux at 1 au for the events in Table 1; the correlation is significant for the combined data set ($r = 0.47$ with $r_c = 0.275$ at 95% confidence level). When MCs and EJs are considered separately, the correlation is still positive but not statistically significant because of the small sample sizes. The regression line for all events $[\Phi_p(1 \, au) = 0.79(\Phi_r)^{1.04}]$ is very close to the equal fluxes line. For $\Phi_r = 10.0 \times 10^{21}$ Mx, the regression line gives $\Phi_p = 8.7 \times 10^{21}$ Mx, which is 13% smaller. The regression line for MCs (based on Lepping et al., 1990 fits) obtained in Gopalswamy et al. (2017) was $1.20(\Phi_r)^{0.85}$, which yields a similar value: $\Phi_p = 8.5 \times 10^{21}$ Mx; the MC regression line (Fig. 7a) gives the same Φ_p.

In Fig. 7b, we show how the axial magnetic field B_0 at 10 Rs is related

to that in the corresponding 1-au flux rope. The combined data set (MC + EJ) shows a reasonable correlation ($r = 0.43$ with $r_c = 0.275$). Taken separately, both MCs and EJs show positive correlation, but the correlations are not statistically significant due to insufficient sample sizes. It is certainly remarkable that quantities derived from completely independent observations made 1 au apart show reasonable correlation. Finally, Fig. 7c shows the correlation between the derived B_0 at 10 Rs and the observed maximum magnetic field strength (B_t) in the corresponding ICMEs. The correlation ($r = 0.51$ with $r_c = 0.243$) is certainly better than that in Fig. 7a and b. The high correlation is promising that the solar eruption data have a high prediction value not only for the arrival time, but also for 1-au magnetic properties, crucial for space weather applications.

5. Discussion

We characterized the dimensions and magnetic content of CME flux ropes near the Sun based on eruption data for a set of more than 50 events. We obtained the geometric properties of CME flux ropes (aspect ratio and the flux rope radius at the apex) by fitting a flux rope to the white-light coronagraphic observations from SOHO/LASCO. Since we had only single view observations during solar cycle 23, we used the EFR model of Krall and St. Cyr (2006). We obtained the magnetic properties of the flux ropes (poloidal flux and axial field strength) using the RC flux in the eruption region; the RC flux itself was determined from the photospheric magnetic flux underlying the post eruption arcades (Gopalswamy et al., 2017). Other properties such as the helicity sign of the flux rope can easily be obtained from the hemispheric rule or using one of a number signatures in the source region, including the skew of the post eruption arcade (e.g., Bothmer and Schwenn, 1998; Yurchyshyn et al., 2001; Yurchyshyn, 2008; Sheeley et al., 2013). For force-free flux ropes, the toroidal flux can be readily obtained from the poloidal flux. Furthermore, one can also obtain the poloidal (B_p) and toroidal (B_a)
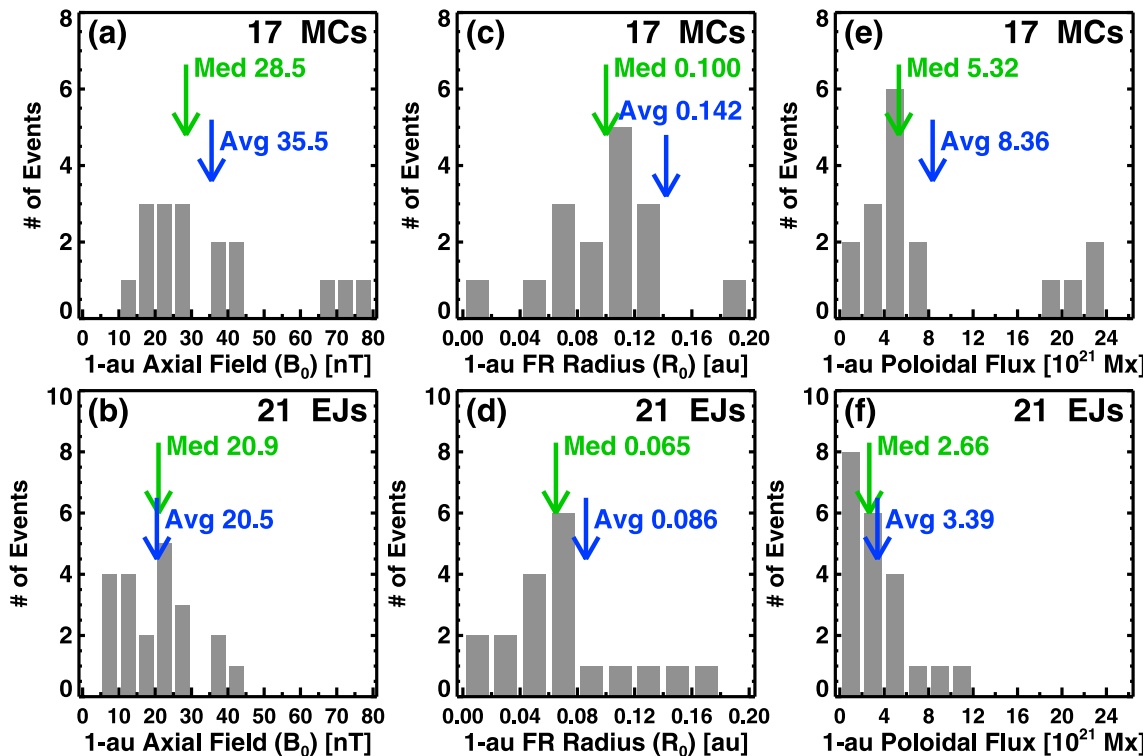
Fig. 6. Distributions of axial magnetic field strength (a,b), the flux-rope (FR) radius (c,d) and the derived flux-rope poloidal flux (e,f) at 1 au. The top and bottom panels show the quantities associated with MCs and EJs, respectively. The mean (Avg) and median (Med) values are indicated on the plots. Kolmogorov-Smirnov test comparing the MC and EJ distributions shows that the difference between the MC and EJ events are significant for the axial field strength (a, b) and the poloidal flux (e,f). The difference is marginal in the case of the radius of the flux rope. The D-statistic for the three parameters (left to right) and the probability (p) that the D value is by chance are: 0.4174 (p = 0.05), 0.3950 (p = 0.08), and 0.4314 (p = 0.04).
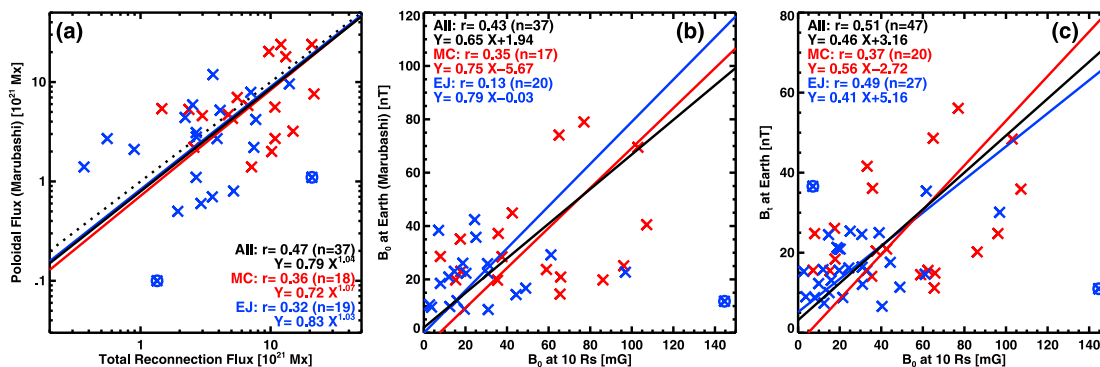
expected, the space speed and axial field strength of the coronal flux ropes have a strong correlation (r = 0.58 with r_c = 0.240 for 48 events; see Fig. 8a). In Fig. 8b we have shown the scatter plot between ICME speed and its peak field strength similar to the plot published by Gonzalez et al. (1998). We see that the correlation is very high (r = 0.73 with r_c = 0.240 for 48 events). It must be noted that the range of speeds and magnetic field strengths in Fig. 8b is much larger than that (<700 km/s, <35 nT) used by Gonzalez et al. (1998). Furthermore, the correlation is significant for both MCs and EJs in Fig. 8b, whereas Gonzalez et al. (1998) found no correlation for EJs. There is also good correlation between the CME space speed in Fig. 8a and the ICME field strength in Fig. 8b, giving a regression line $B_t = 0.012V_{sp} + 7.0$, with a correlation coefficient of 0.65. We can conclude that a flux rope with higher initial speed (or kinetic energy) is indicative of a flux rope with a larger magnetic content, ultimately stemming from the RC flux. This can also be seen from the correlation between CME space speed and the ICME magnetic field strength.

One of the significant findings of this study is that while both MC and EJ type ICMEs have flux rope structure, there are some differences in the flux rope properties. However, the difference is certainly not flux rope (MC) vs. non-rope (EJ) structure as was suggested by some authors (e.g., Gosling, 1990). Gosling (1990) suggested that the EJ events may be non-ropes, i.e., the field lines simply expand from the source region without the helical structure. However, such expansion would not involve reconnection and therefore no post eruption arcades or flux ropes would be involved. We have shown that both MC and EJ type ICMEs have similar arcade structure at the Sun and charge states at 1 au implying flare association (Yashiro et al., 2013; Gopalswamy et al., 2013b). We showed that the difference between the MC and EJ source regions is in terms of the amount of RC flux involved, resulting in a weaker magnetic content of the coronal and 1-au flux ropes.

6. Conclusions

We have shown that it is possible to fully characterize the geometrical and magnetic properties of CME flux ropes ejected from the Sun soon after the eruption. The flux rope can then be input to global MHD models for prediction purposes. The main conclusions of this study are:

1. In order to obtain the RC flux in an eruption, we need the following information: (i) post-eruption arcades from EUV or soft X-rays and (ii) a photospheric magnetogram taken near the eruption time.
2. A coronal flux rope can be constructed by combining the geometric properties of the flux rope obtained from coronagraph images and the magnetic properties derived from the RC flux under the assumption of a force-free flux rope.
3. The RC flux is well correlated with flare size, flare fluence, CME speed, CME width, CME kinetic energy, and 1-au magnetic field strength of the flux rope associated with the CME.
4. The RC flux in the source regions of MC- and EJ-type ICMEs is significantly different. The flux ropes in EJ events have a smaller magnetic content (lower axial field strength and poloidal flux) compared to those in MCs. This is true near the Sun and at 1 au.
5. The magnetic field strength in coronal flux ropes is higher than that in the ambient corona by a factor of 2.8 for MCs and 1.8 for EJs. This can be tested using direct observations to be obtained by the Solar Probe Plus mission.
6. The magnetic field strength in a coronal flux rope falls faster than the ambient field strength, due to the expansion resulting from higher internal magnetic pressure. This is also reflected in the larger flux rope size at 1 AU in MCs than in EJs.
7. The relation between the RC flux and the poloidal flux of 1-au flux ropes obtained previously for MC events also holds when the EJ events are included.
8. The high correlation between the coronal flux ropes constructed from eruption data and the 1-au flux ropes constructed from in situ data

suggests that one can improve the space weather prediction by providing realistic input to global MHD models.
9. The approximate equality between the flare RC flux and the poloidal flux of the flux rope formed due to reconnection, strongly suggests that a pre-eruption flux rope may not exist.

Author contributions

N. Gopalswamy conceived the project, participated in the data analysis and interpretation of the results, and drafted the manuscript. S. Akiyama performed correlation analysis and created some of the figures. S. Yashiro performed data analysis and created some figures. H. Xie fitted flux ropes to the coronagraph data and obtained the flux rope parameters.

References

Acuña, M.H., Ogilvie, K.W., Baker, D.N., et al., 1995. The global geospace science program and its investigations. SSRv 71, 5.

Bothmer, V., Schwenn, R., 1998. The structure and origin of magnetic clouds in the solar wind. Ann. Geo 16, 1.

Brueckner, G.E., Howard, R.A., Koomen, M.J., Korendyke, C.M., Michels, D.J., Moses, J.D., 1995. The large angle spectroscopic coronagraph (LASCO). Sol. Phys. 162, 357–402.

Burlaga, L.F., Sittler, E., Mariani, F., Schwenn, R., 1981. Magnetic loop behind an interplanetary shock: voyager, Helios, and IMP-8 observations. J. Geophys. Res. 86, 6673.

Carmichael, H., 1964. A process for flares. In: Hess, W.N. (Ed.), Physics of Solar Flares, NASA SP-50, Washington DC, 451.

Chen, J., Howard, R.A., Brueckner, G.E., Santoro, R., Krall, J., Paswaters, S.E., St. Cyr, O.C., Schwenn, R., Lamy, P., Simnett, G.M., 1997. Evidence of an erupting magnetic flux rope: LASCO coronal mass ejection of 1997 April 13. ApJ 490, L191–L194.

Delaboudinière, J.-P., Artzner, G.E., Brunaud, J., et al., 1995. EIT: extreme-ultraviolet imaging telescope for the SOHO mission. Sol. Phys. 162, 291.

Démoulin, P., Dasso, S., Owens, M.J., Sauvaud, J.-A., Rouillard, A.P., Lynnyk, A., Foullon, C., Savani, N.P., Luhmann, J.G., Galvin, A.B., 2015. Statistical study of magnetic cloud erosion by magnetic reconnection. JGRA 120, 43.

Domingo, V., Fleck, B., Poland, A.I., 1995. The SOHO mission: an overview. Sol. Phys. 162, 1.

Forbes, T.G., 2000. A review on the genesis of coronal mass ejections. JGR 105, 23153.

Gibson, S.E., Low, B.C., 1998. A time-dependent three-dimensional magnetohydrodynamic model of the coronal mass ejection. ApJ 493, 460.

Goldstein, H., 1983. On the field configuration in magnetic clouds. In: JPL Solar Wind Five, pp. 731–733.

Gonzalez, W.D., Tsurutani, B.T., 1987. Criteria of interplanetary parameters causing intense magnetic storms (Dst < 100 nT). Planet Space Sci. 35, 1101–1109.

Gonzalez, W.D., Clúa De Gonzalez, L., Dal Lago, A., Tsurutani, B.T., Arballo, J.K., Lakhina, G.S., Buti, B., Ho, G.M., 1998. Magnetic cloud field intensities and solar wind velocities. GRL 25, 963.

Gopalswamy, N., 2006. Properties of interplanetary coronal mass ejections. Space Sci. Rev. 124, 145.

Gopalswamy, N., 2008. Solar connections of geoeffective magnetic structures. JASTP 70, 2078–2100.

Gopalswamy, N., 2009. Coronal mass ejections and space weather. In: Tsuda, T., Fujii, R., Shibata, K., Geller, M.A. (Eds.), Climate and Weather of the Sun-earth System (CAWSES): Selected Papers from the 2007 Kyoto Symposium. Terrapub, Tokyo, p. 77.

Gopalswamy, N., Xie, H., Mäkelä, P., Akiyama, S., Yashiro, S., Kaiser, M.L., Howard, R.A., Bougeret, J.-L., 2010. Interplanetary Shocks Lacking Type II Radio Bursts. ApJ 710, 1111.

Gopalswamy, N., 2010a. The CME link to geomagnetic storms. In: Kosovichev, A.G., Andrei, A.H., Rozelot, J.-P. (Eds.), Solar and Stellar Variability: Impact on Earth and Planets., Proc. IAU Symposium No. 264, p. 326.

Gopalswamy, N., 2010b. Coronal mass ejections: a summary of recent results. In: Proc. Of the 20th National Solar Physics Meeting, Held 31 May - 4 June, 2010 in Papradno, Slovakia, pp. 108–130.

Gopalswamy, N., 2011. Coronal mass ejections and their heliospheric consequences. In: Rai Choudhuri, A., Banerjee, D. (Eds.), ASI Conference Series, vol. 2, pp. 241–258.

Gopalswamy, N., Yashiro, S., 2011. The strength and radial profile of the coronal magnetic field from the standoff distance of a coronal mass ejection-driven shock. ApJ 736, L17.

Gopalswamy, N., Lara, A., Lepping, R.P., Kaiser, M.L., Berdichevsky, D., St. Cyr, O.C., 2000. Interplanetary acceleration of coronal mass ejections. GRL 27, 145.

Gopalswamy, N., Lara, A., Yashiro, S., Kaiser, M.L., Howard, R.A., 2001. Predicting the 1-AU arrival times of coronal mass ejections. JGR 106, 29207.

Gopalswamy, N., Yashiro, S., Liu, Y., Michalek, G., Vourlidas, A., Kaiser, M.L., Howard, R.A., 2005a. Coronal mass ejections and other extreme characteristics of the 2003 october-November solar eruptions. JGRA 110, A09S15.

Gopalswamy, N., Aguilar-Rodriguez, E., Yashiro, S., Nunes, S., Kaiser, M.L., Howard, R.A., 2005b. Type II radio bursts and energetic solar eruptions. JGRA 110, 12S07.

Gopalswamy, N., Akiyama, S., Yashiro, S., Michalek, G., Lepping, R.P., 2008. Solar sources and geospace consequences of interplanetary magnetic clouds observed during solar cycle 23. JASTP 70, 245.

Gopalswamy, N., Akiyama, S., Yashiro, S., 2009a. Major solar flares without coronal mass ejections. In: Gopalswamy, N., Webb, D.F. (Eds.), Universal Heliophysical Processes, Proc. International Astronomical Union, IAU Symposium, vol. 257, pp. 283–286.

Gopalswamy, N., Yashiro, S., Michalek, G., Stenborg, G., Vourlidas, A., Freeland, S., Howard, R., 2009b. The SOHO/LASCO CME catalog. Earth, Moon Planets 104, 295–313.

Gopalswamy, N., Mäkelä, P., Xie, H., Akiyama, S., Yashiro, S., 2009c. CME interactions with coronal holes and their interplanetary consequences. JGRA 114, A00A22.

Gopalswamy, N., Akiyama, S., Yashiro, S., Mäkelä, P., 2010a. Coronal mass ejections from sunspot and non-sunspot regions. In: Hasan, S.S., Rutten, R.J. (Eds.), Magnetic Coupling between the Interior and Atmosphere of the Sun, Astrophysics and Space Science Proceedings. Springer, Berlin Heidelberg, pp. 289–307.

Gopalswamy, N., Xie, H., Mäkelä, P., Akiyama, S., Yashiro, S., Kaiser, M.L., Howard, R.A., Bougeret, J.-L., 2010b. Interplanetary shocks lacking type II radio bursts. Astrophys. J. 710, 1111.

Gopalswamy, N., Mäkelä, P., Akiyama, S., Xie, H., Yashiro, S., Reinard, A.A., 2013. The solar connection of enhanced heavy ion charge states in the interplanetary medium: implications for the flux-rope structure of CMEs. Sol. Phys. 284, 17.

Gopalswamy, N., Nieves-Chinchilla, T., Hidalgo, M., Zhang, J., Riley, P., van Driel-Gesztelyi, L., Mandrini, C.H., 2013a. Preface. Sol. Phys. 284, 1.

Gopalswamy, N., Mäkelä, P., Akiyama, S., Xie, H., Yashiro, S., Reinard, A.A., 2013b. The solar connection of enhanced heavy ion charge states in the interplanetary medium: implications for the flux-rope structure of CMEs. Sol. Phys. 284, 17.

Gopalswamy, N., Xie, H., Akiyama, S., Mäkelä, P.A., Yashiro, S., 2014a. Major solar eruptions and high-energy particle events during solar cycle 24. Earth, Planets Space 66, 104.

Gopalswamy, N., Akiyama, S., Yashiro, S., Xie, H., Mäkelä, P., Michalek, G., 2014b. Anomalous expansion of coronal mass ejections during solar cycle 24 and its space weather implications. GRL 41, 2673.

Gopalswamy, N., Xie, H., Akiyama, S., Mäkelä, P., Yashiro, S., Michalek, G., 2015a. the peculiar Behavior of halo coronal mass ejections in solar cycle 24. ApJ 804, L23.

Gopalswamy, N., Mäkelä, P., Akiyama, S., Yashiro, S., Xie, H., Thakur, N., Kahler, S.W., 2015b. Large solar energetic particle events associated with filament eruptions outside of active regions. ApJ 806, 8.

Gopalswamy, N., Yashiro, S., Xie, H., Akiyama, S., Mäkelä, P., 2015c. Properties and geoeffectiveness of magnetic clouds during solar cycles 23 and 24. JGRA 120, 9221.

Gopalswamy, N., Yashiro, S., Akiyama, S., Xie, H., 2017. Estimation of reconnection flux using post-eruption arcades and its relevance to 1-AU magnetic clouds. Sol. Phys. 292, 65.

Gosling, J.T., 1990. Coronal mass ejections and magnetic flux ropes in interplanetary space. In: Russell, C.T., Priest, E.R., Lee, L.C. (Eds.), Physics of Magnetic Flux Ropes, Geophys. Monogr. Ser. 58, AGU, Washington DC, 343.

Hirayama, T., 1974. Theoretical model of flares and prominences. I: evaporating flare model. Sol. Phys. 34, 323.

Hu, Q., Qiu, J., Dasgupta, B., Khare, A., Webb, G.M., 2014. Structures of interplanetary magnetic flux ropes and comparison with their solar sources. ApJ 793, 53.

Jin, M., Manchester, W.B., van der Holst, B., Sokolov, I., Tóth, G., Vourlidas, A., de Koning, C.A., Gombosi, T.I., 2017a. Chromosphere to 1 AU simulation of the 2011 March 7th event: a comprehensive study of coronal mass ejection propagation. ApJ 834, 172.

Jin, M., Manchester, W.B., van der Holst, B., Sokolov, I., Tóth, G., Mullinix, R.E., Taktakishvili, A., Chulaki, A., Gombosi, T.I., 2017b. Data-constrained coronal mass ejections in a global magnetohydrodynamics model. ApJ 834, 173.

Kaiser, M.L., Kucera, T.A., Davila, J.J., et al., 2008. The STEREO mission: an introduction. SSRv 136, 5.

Kim, R.-S., Gopalswamy, N., Cho, K.-S., Moon, Y.-J., Yashiro, S., 2013. Propagation characteristics of CMEs associated with magnetic clouds and ejecta. Sol. Phys. 284, 77.

Klein, L.W., Burlaga, L.F., 1982. Interplanetary magnetic clouds at 1 AU. JGRA 87, 613.

Kopp, R.A., Pneuman, G.W., 1976. Magnetic reconnection in the corona and the loop prominence phenomenon. Sol. Phys. 50, 85.

Krall, J., 2007. Are all coronal mass ejections hollow flux ropes? ApJ 657, 559.

Krall, J., St. Cyr, O.C., 2006. Flux-rope coronal mass ejection geometry and its relation to observed morphology. Astrophys. J. 652, 1740.

Lepping, R.P., Burlaga, L.F., Jones, J.A., 1990. Magnetic field structure of interplanetary magnetic clouds at 1 AU. JGRA 95, 11957–11965.

Lepping, R.P., et al., 1995. The wind magnetic field investigation. SSRv 71, 207.

Lindsay, G.M., Luhmann, J.G., Russell, C.T., Gosling, J.T., 1999. Relationships between coronal mass ejection speeds from coronagraph images and interplanetary characteristics of associated interplanetary coronal mass ejections. JGRA 104, 12515.

Longcope, D., Beveridge, C., Qiu, J., Ravindra, B., Barnes, G., Dasso, S., 2007. Modeling and measuring the flux reconnected and ejected by the two-ribbon flare/CME event on 7 November 2004. Sol. Phys. 244, 45.

Mackay, D.H., Gaizauskas, V., Rickard, G.J., Priest, E.R., 1997. ApJ 486, 534.

Mäkelä, P., Gopalswamy, N., Xie, H., Mohamed, A.A., Akiyama, S., Yashiro, S., 2013. Coronal hole influence on the observed structure of interplanetary CMEs. Sol. Phys. 284, 59.

Manchester, W.B., Kozyra, J.U., Lepri, S.T., Lavraud, B., 2014. Simulation of magnetic cloud erosion during propagation. JGRA 119, 5449.

Marubashi, K., 1997. Interplanetary magnetic flux ropes and solar filaments. In: Crooker, N., Joselyn, J.A., Feynman, J. (Eds.), Coronal Mass Ejections. Geophysical Monograph Series 99. American Geophysical Union, Washington DC, pp. 147–156.

Marubashi, K., Akiyama, S., Yashiro, S., Gopalswamy, N., Cho, K.-S., Park, Y.-D., 2015. Geomagnetic relationship between interplanetary flux ropes and their solar sources. Sol. Phys. 290, 1371.

Metcalf, T.R., Jiao, L., McClymont, A.N., Canfield, R.C., Uitenbroek, H., 1995. Is the solar chromospheric magnetic field force-free? ApJ 439, 474.

Moore, R.L., Sterling, A.C., Suess, S.T., 2007. The width of a solar coronal mass ejection and the source of the driving magnetic explosion: a test of the standard scenario for CME production. ApJ 668, 1221.

Möstl, C., Farrugia, C.J., Miklenic, C., Temmer, M., Galvin, A.B., Luhmann, J.G., Kilpua, E.K.J., Leitner, M., Nieves-Chinchilla, T., Veronig, A., Biernat, H.K., 2009. Multispacecraft recovery of a magnetic cloud and its origin from magnetic reconnection on the Sun. JGRA 114, A04102.

Mouschovias, T.C., Poland, A.I., 1978. Expansion and broadening of coronal loop transients: a theoretical explanation. ApJ 220, 675.

Owens, M.J., Cargill, P.J., Pagel, C., Siscoe, G.L., Crooker, N.U., 2005. Characteristic magnetic field and speed properties of interplanetary coronal mass ejections and their sheath regions. JGR 110, A01105.

Qiu, J., Hu, Q., Howard, T.A., Yurchyshyn, V.B., 2007. On the magnetic flux budget in low-corona magnetic reconnection and interplanetary coronal mass ejections. ApJ 659, 758.

Ruffenach, A., Lavraud, B., Farrugia, C.J., et al., 2015. Statistical study of magnetic cloud erosion by magnetic reconnection. JGRA 120, 43–60.

Scherrer, P.H., Bogart, R.S., Bush, R.I., et al., 1995. The solar oscillations investigation - Michelson doppler imager. Sol. Phys. 162, 129.

Sheeley Jr., N.R., Martin, S.F., Panasenco, O., Warren, H.P., 2013. Using coronal cells to infer the magnetic field structure and chirality of filament channels. ApJ 722, 88.

Shibata, K., Masuda, S., Shimojo, M., Hara, H., Yokoyama, T., Tsuneta, S., Kosugi, T., Ogawara, Y., 1995. Hot-plasma ejections associated with compact-loop solar flares. ApJ 451, L83.

Stone, E.C., Frandsen, A.M., Mewaldt, R.A., Christian, E.R., Margolies, D., Ormes, J.F., Snow, F., 1998. The advance composition explorer. SSRv 86, 1.

Sturrock, P.A., 1966. Model of the high-energy phase of solar flares. Nature 211, 695.

Thernisien, A., 2011. Implementation of the graduated cylindrical shell model for the three-dimensional reconstruction of coronal mass ejections. ApJS 194, 33.

Tóth, G., de Zeeuw, D.L., Gombosi, T.I., Manchester, W.B., Ridley, A.J., Sokolov, I.V., Roussev, I.I., 2007. Sun-to-thermosphere simulation of the 28-30 october 2003 storm with the space weather modeling framework. Space Weather 5 (06003).

Tsuneta, S., Acton, L., Bruner, M., Lemen, J., Brown, W., Caravalho, R., Catura, R., Freeland, S., Jurcevich, B., Morrison, M., Ogawara, Y., Hirayama, T., Owens, J., 1991. The soft X-ray telescope for the SOLAR-a mission. Sol. Phys. 136, 37.

Wilson, R.M., 1987. Geomagnetic response to magnetic clouds. Planet Space Sci. 35, 329.

Wu, C.-C., Lepping, R.P., 2002. The Effects of Magnetic Clouds on the Occurrences of Geomagnetic Storms. 107, SSH 3–1, CiteID 1346.

Xie, H., Ofman, L., Lawrence, G., 2004. Cone model for halo CMEs: application to space weather forecasting. JGR 109, 3109.

Xie, H., Gopalswamy, N., St. Cyr, O.C., 2013. Near-sun flux rope structure of CMEs. Sol. Phys. 284, 47.

Yashiro, S., Gopalswamy, N., Michalek, G., St.Cyr, O.C., Plunkett, S.P., Rich, N.B., Howard, R.A., 2004. JGRA 109, A07105.

Yashiro, S., Gopalswamy, N., Mäkelä, P., Akiyama, S., 2013. Post-eruption arcades and interplanetary coronal mass ejections. Sol. Phys. 284, 5.

Yurchyshyn, V., 2008. Relationship between EIT post-eruption arcades, coronal mass ejections, the coronal neutral line, and magnetic clouds. ApJ 675, L49.

Yurchyshyn, V.B., Wang, H., Goode, P.R., Deng, Y., 2001. Orientation of the magnetic fields in interplanetary flux ropes and solar filaments. APJ 563, 381.

Zhang, J., Richardson, I.G., Webb, D.F., Gopalswamy, N., Huttunen, E., Kasper, J., Nitta, N.V., Poomvises, W., Thompson, B.J., Wu, C.-C., Yashiro, S., Zhukov, A.N., 2007. Solar and interplanetary sources of geomagnetic storms (Dst ≤ -100 nT). JGRA 112, A10102.